Monocular Deformable Model-to-Image Registration of Vascular Structures

Martin Groher, Maximilian Baust, Darko Zikic, and Nassir Navab

Computer Aided Medical Procedures (CAMP),
Technische Universität München, Germany

Abstract. The registration of 3D vasculature to 2D projections is the key for providing advanced systems for image-based navigation and guidance. In areas with non-rigid patient motion, however, it is very difficult to accurately perform the registration if only one 2D view is available.

We propose a method for deformable registration of a 3D vascular model extracted from an angiographic scan to a single 2D Digitally Subtracted Angiogram (DSA). Different to existing approaches, our method does not require a segmentation of 2D vasculature. In consequence, our method can be used without manual interaction during medical treatment.

Formulated as an energy minimization problem, our approach combines a novel data term with the length regularization proposed in [1] which removes the ill-posedness of this monocular scenario. Besides attracting projected 3D centerline points to locations with high vessel probability the proposed data term ensures an injective projection of the centerline points.

Due to our novel image-based data term, we achieve a considerable gain in performance compared to feature-based approaches.

Accuracy, robustness to outliers, as well as performance issues are analyzed through tests on synthetic and real data within a controlled environment.

1 Introduction

Image-based guidance on angiographic images has become a standard technique in modern hospitals. Needles, catheters, guide wires, or other instruments are injected into the patient vessel system and their progression is usually monitored by 2D angiography and fluoroscopy. Most procedures are carried out with a mono-plane device, which produces 2D images from one view only. Efforts have been made to bring 3D angiographic scans into the 2D guidance process in order to constantly provide spatial details on vasculature [2,3].

One of the main obstacles to be overcome here is an accurate 2D-3D registration of vessel images. Only then, a correct fusion of the available information can create a benefit in terms of depth perception or augmentation. Especially in abdominal or cardiac procedures, vessels are subject to non-rigid motion, which has to be considered by the registration process.

B. Fischer, B. Dawant, and C. Lorenz (Eds.): WBIR 2010, LNCS 6204, pp. 37–47, 2010.

While rigid 2D-3D vessel registration has been addressed extensively in the literature [4,5,6,7], deformable registration is mostly tackled only if multi-plane X-ray devices are available [8,9,10]. For a single view scenario, a method has been proposed recently, which aligns centerline features of 3D vasculature by minimizing the Euclidean distance of projected centerline points to their nearest 2D pendants [1]. The data term alone cannot solve for displacements in projection direction. By adding a length preservation together with a smoothing regularization term this issue is met and the registration is driven to the accurate solution.

This approach successfully recovers a non-rigid transformation from only one view, but requires an extraction of centerline features in 3D and in 2D. Due to a uniform contrast propagation, the 3D extraction can be carried out with quite simple processing methods; 2D angiograms, however, include regions with inhomogeneous contrast distribution and vessel overlays, which may lead to erroneous results when creating a vascular model. Moreover, such extraction techniques often require a certain amount of user interaction, which is undesired during medical procedures.

We address this issue by proposing a method which registers a 3D vascular model to a vessel image, e.g. a DSA, without any prior geometric extraction step in 2D. To this end, we define a circular region around each projected centerline point in which intensities of the 2D image are accumulated. The region is formalized using a level set function, which inherently penalizes solutions where multiple regions project onto the same part of the image. The accumulated intensities, together with a length preservation in 3D, define an energy, whose optimization attracts projected centerline points towards 2D vessel centers. In order to keep our computed transformations smooth we regularize the updates of a gradient descent scheme using approximating thin-plate splines [11,12].

Tests on synthetic examples and a comparison with the feature-based approach from [1] show the high accuracy as well as the improved runtime of our approach. Additional to the synthetic data, we conduct an experiment with patient data, where two 3D data sets are available, one preoperative Computed Tomography Angiogram (CTA) and an intraoperative 3D reconstruction.

2 Method

Our method optimizes an energy, which is defined on a vascular model extracted from a 3D angiographic scan, a 2D image where noise is reduced and tubular structures are enhanced, and a projection function, which relates each 3D point to a corresponding 2D point in the image plane.

In order to create the vascular model consisting of centerline points and their associated radii, a region growing algorithm is applied to the 3D data. Due to uniform contrast propagation, this basic method yields a good segmentation result, which is used to compute centerline points (via a topological thinning algorithm) and associated radii (via a Euclidean distance transformation), see Fig. 1.

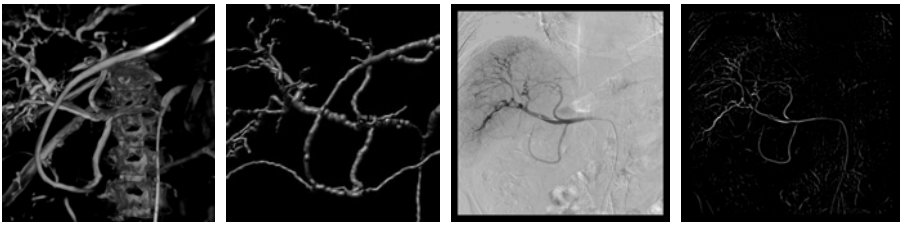

Fig. 1. From left to right: 3D input volume showing liver arteries and spine; 3D vascular model, where centerline points and radii are extracted from the input volume; 2D DSA of the same patient; 2D DSA with enhanced tubular structures

For noise reduction and vessel enhancement of the 2D DSA we use a filter which enhances tubular structures in a multi-scale approach [13]. This is accomplished by a pixel-wise comparison of the gradient vector and the eigenvector of the Hessian associated to the larger eigenvalue at a distance equal to the expected radius of the vessel. The more parallel the two vectors, the higher the response of the filter, compare Fig. 1.

The projection parameters are assumed to be given by the device. This is achieved either by machine-based geometric calibration [2], or by a rigid registration step [6], which is carried out prior to the deformable registration.

2.1 Energy Formulation

Let $\{\mathbf{X}_i\}$ be the set of n centerline points in 3D. Each centerline point $\mathbf{X}_i$ has an associated vessel radius R_i. We denote our vascular model with the tuples $\{(\mathbf{X}_i, R_i)\}$. For each $\mathbf{X}_i$ we define a displacement vector φ_i and a displaced location $\mathbf{Y}_i = \mathbf{X}_i + \varphi_i$. The vector including all entries of the displacement vectors φ_i is denoted by φ.

Now we want to find the displacement φ' minimizing the following energy:

$$\varphi' = \arg\min_{\varphi} E_E \; + \; \alpha E_I, \tag{1}$$

where E_E defines the external energy, and E_I represents the internal (regularizing) energy. The weighting parameter α controls the impact of the regularization.

External Energy. Let $p : \mathbb{R}^3 \rightarrow \mathbb{R}^2$ be a perspective projection function. We denote projected centerline points by $\mathbf{x}_i = p(\mathbf{X}_i)$ and their projected radii by $r_i = ||p(\mathbf{X}_i) - p(\mathbf{X}_i + R_i\mathbf{V})||$, where $\mathbf{V}$ is a 3D unit vector parallel to the image plane in device coordinates[1].

We want to encourage each 3D centerline point $\mathbf{X}_i$ to project onto the center of a 2D vessel. As centerline points correspond to high values in the enhanced

[1] The device coordinate system has its origin in the center of projection, spans the x-y-plane parallel to the image plane and the z-axis points towards the image plane. If p is described by a projection matrix $\mathtt{P} = \mathtt{K}[\mathtt{R}|\mathbf{t}] \in \mathbb{R}^{3\times4}$, world coordinates are transformed to device coordinates by applying rotation $\mathtt{R}$ and translation $\mathbf{t}$.

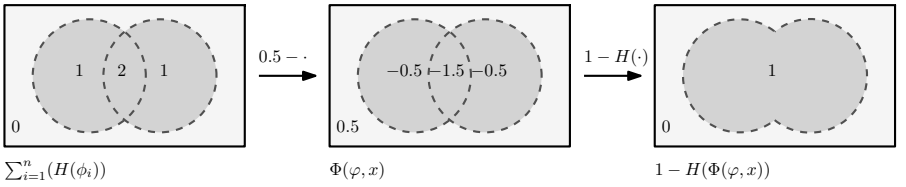

Fig. 2. illustration of the selection term of Eq. (7)

2D image $\mathcal{I}_f : \Omega \subseteq \mathbb{R}^2 \rightarrow \mathbb{R}$ (Fig. 1) the following data term seems to be a reasonable choice:

$$\widehat{E}_E(\varphi) = -\sum_{i=1}^{n} \int_{D_i} \mathcal{I}_f(\mathbf{x})\, d\mathbf{x}, \tag{2}$$

where $D_i = D(p(\mathbf{X}_i + \varphi_i), r_i)$ denotes the disk with radius r_i centered at the ith projected centerline point. In order to obtain a formulation where the integration domain is independent of φ_i and r_i we rewrite $\widehat{E}_E$ in terms of level set functions:

$$\widehat{E}_E(\varphi) = -\sum_{i=1}^{n} \int_{\Omega} \mathcal{I}_f(\mathbf{x}) \cdot H(\phi_i(\mathbf{x}))\, d\mathbf{x}, \tag{3}$$

where

$$\phi_i(\mathbf{x}) = r_i - \|\mathbf{x} - p(\mathbf{X}_i + \varphi_i)\| \tag{4}$$

is a level set function whose zero level set is the boundary of the disk D_i and

$$H(x) = \begin{cases} 0, & x \leq 0, \\ 1, & x > 0, \end{cases} \tag{5}$$

denotes the Heaviside function. Unfortunately $\widehat{E}_E$ does not prevent all centerline points from being projected onto the same point in 2D, because the area of the projected disks $\sum_i \int_\Omega H(\phi_i)$ is always constant regardless of the position of the projected points $p(\mathbf{X}_i + \varphi_i)$. Consequently an overlap of the disks D_i is not penalized by $\widehat{E}_E$. In order to resolve this issue we define the level set function

$$\Phi(\mathbf{x}, \varphi) = 0.5 - \sum_{i=1}^{n} H(\phi_i(\mathbf{x})). \tag{6}$$

Now the area $\int_\Omega 1 - H(\Phi)$ defined by Φ shrinks when the projected disks D_i overlap as depicted in Fig. 2. Thus an improved data term is given by

$$E_E(\varphi) = -\int_{\Omega} \mathcal{I}_f(\mathbf{x}) \cdot (1 - H(\Phi(\mathbf{x}, \varphi)))\, d\mathbf{x}. \tag{7}$$

Internal Energy. Similar to [1] we add a length preservation term to induce transformations in projection direction. To each centerline point $\mathbf{X}_i$ we define a squared distance to left and right centerline neighbors, denoted by $d(\mathbf{X}_i, \mathbf{X}_{i\pm1})$. E_I is then given by the relative change in length after deformation

$$E_I = \frac{1}{n}\sum_{i=1}^{n}\left[\frac{d(\mathbf{X}_i, \mathbf{X}_{i\pm1}) - d(\mathbf{Y}_i, \mathbf{Y}_{i\pm1})}{d(\mathbf{X}_i, \mathbf{X}_{i\pm1})}\right]^2, \tag{8}$$

where $\mathbf{Y}_i = \mathbf{X}_i + \varphi$ as defined above. To impose transformation smoothness, there are two approaches that can be followed in general. Either a penalizing term is added to the internal energy, or a regularizing operator is directly applied to the updates that are computed in the optimization procedure [12]. We choose the second approach, and realize it by computing an *approximating* thin-plate spline (TPS) from the displacement updates in each iteration. The displacements are then smoothed by recalculating their values from the TPS. By choosing the TPS basis function $U(r) = -|r|$ we minimize the second derivatives of the 3D displacement field [14].

2.2 Optimization

We employ two different gradient-based optimization methods. One is a steepest descent approach, the second is a BFGS optimization [15], which usually yields faster convergence.

The first derivative of E_E with respect to parameters φ_k is given by

$$\frac{\partial E_E}{\partial \varphi_k} = -\int_\Omega \mathcal{I}_f(\mathbf{x})\delta(\Phi(\mathbf{x},\varphi))\delta(r_k - ||\mathbf{x} - p(\mathbf{Y}_k)||)\frac{(\mathbf{x} - p(\mathbf{Y}_k))^\top}{||\mathbf{x} - p(\mathbf{Y}_k)||}\mathtt{J}(\mathbf{Y}_k)\, d\mathbf{x}, \tag{9}$$

where $\mathtt{J}(\mathbf{Y}_k) \in \mathbb{R}^{2\times3}$ is the Jacobian of the projection function p evaluated at $\mathbf{Y}_k$, and δ is the Dirac delta-function.

The first derivative of E_I with respect to parameters φ_k is given by

$$\frac{\partial E_I}{\partial \varphi_k} = -\frac{8}{n}[\kappa_k^-(\mathbf{Y}_k - \mathbf{Y}_{k-1}) + \kappa_k^+(\mathbf{Y}_k - \mathbf{Y}_{k+1})], \tag{10}$$

where $\kappa_k^\pm = (d(\mathbf{X}_k, \mathbf{X}_{k\pm1}) - d(\mathbf{Y}_i, \mathbf{Y}_{k\pm1}))/d(\mathbf{X}_i, \mathbf{X}_{k\pm1})$ [1].

The gradients of external and internal energy are normalized such that the gradient of φ_j, which has the highest magnitude is normalized to one:

$$\frac{\partial}{\partial\varphi_k}E_E / \max_{j=1\ldots n}||\frac{\partial}{\partial\varphi_j}E_E|| \text{ , and } \frac{\partial}{\partial\varphi_k}E_I / \max_{j=1\ldots n}||\frac{\partial}{\partial\varphi_j}E_I||. \tag{11}$$

With this, we ensure normalization throughout different units (E_E is computed on image intensities in 2D space, E_I is computed in 3D space), which makes a combination of the two energy terms more tractable. Given the partial derivatives, our registration algorithm can be summarized in Algorithm 1.

Algorithm 1 Monocular Deformable 2D-3D Registration

INPUT: Given a vascular model $\{(\mathbf{X}_i, R_i)\}$, $i = 1, \ldots, n$, an enhanced image $\mathcal{I}$, and a projection function p
OUTPUT: A transformation φ

1: $\varphi_0 = \mathbf{0}$
2: **repeat**
3: compute gradients $\nabla E = \nabla E_E + \alpha \nabla E_I$ using Eqs. (9), (10), and (11)
4: compute update $\Delta\varphi$ using gradient direction
5: compute TPS warp $\mathbf{W}$ given $\{\mathbf{X}_i\}$,$\{\mathbf{X}_i + \Delta\varphi_i\}$, $i = 1, \ldots, n$ and a smoothing parameter λ
6: smooth displacement update using warp: $\Delta\tilde{\varphi} = \mathbf{W}(\mathbf{X}_i) - \mathbf{X}_i$
7: $\varphi_{t+1} = \varphi_t + \Delta\tilde{\varphi}$
8: **until** convergence

2.3 Implementation

In our implementation we use smeared-out versions of Heaviside and Dirac delta-function as described in [16], i.e.

$$H(x) = \begin{cases} 0, & x < -\epsilon, \\ \frac{1}{2} + \frac{x}{2\epsilon} + \frac{1}{2\pi} \sin\left(\frac{\pi x}{\epsilon}\right), & -\epsilon \geq x \geq \epsilon, \\ 1, & \epsilon < x, \end{cases} \tag{12}$$

and

$$\delta(x) = \begin{cases} \frac{1}{2\epsilon} + \frac{1}{2\epsilon} \cos\left(\frac{\pi x}{\epsilon}\right), & |x| \leq \epsilon, \\ 0, & |x| > \epsilon. \end{cases} \tag{13}$$

In Eqs. (12) and (13) ϵ is set to 1.5 [16]. We follow the description of the BFGS optimization procedure from [15]. For increasing the capture range of our algorithm we use an image pyramid, which is traversed during optimization. For each pyramid level we update the projection matrix by multiplying $\mathtt{D} = \mathrm{diag}(0.5, 0.5, 1) \in \mathbb{R}^{3\times3}$ from the left. Instead of evaluating the gradient at every pixel in the image domain, we use a narrow band technique, whose boundaries are given by the radii around each projected centerline point.

3 Evaluation

We evaluate our algorithm through tests on synthetic and real data. Artificial data is created such that contains a deformation component in projection direction. We analyze two error measures. The first is the mean Euclidean distance to a ground truth vascular model in 3D. The second error is the deviation from angles defined between vectors to neighboring points in the vascular model. Again, the deviation from the ground truth values is computed. Finally, we compare our method to the feature-based approach [1] in terms of accuracy and runtime. Runtime is evaluated on an Intel Core2Duo 2.6GHz machine. We were kindly provided with data and code by the authors of [1].

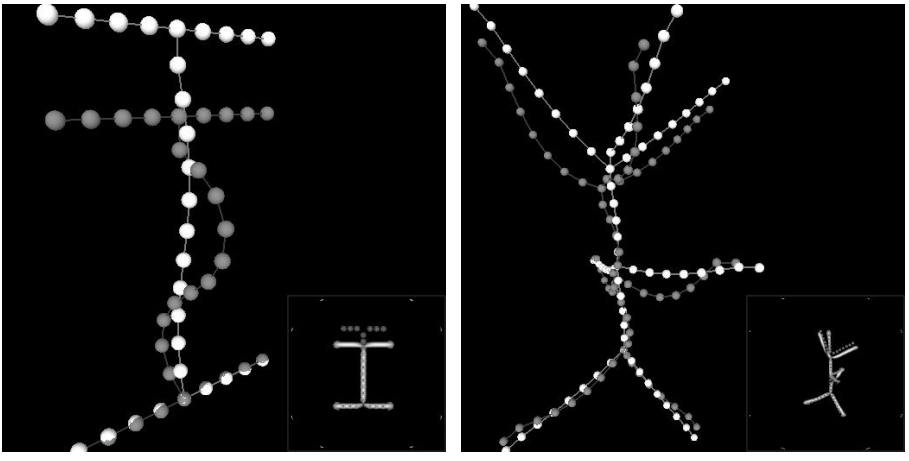

Fig. 3. Two synthetic data sets, denoted S2 and S3 in table 1. The white spheres represent the input vascular model, the gray spheres show the deformed input model (the ground truth) from which the projection image has been generated. The lower right sub-images visualize the enhanced projection images, where dark gray disks are drawn at all projected centerline points at the beginning of the registration.

In all our experiments the input 2D image is enhanced as described in Sec. 2. This fully automatic filter takes approximately 3 *sec* on an image of size 1024×1024 pixels. The parameter α, which controls the length preservation term, is set between 0.5 and 2.0, the smoothing parameter λ (see Algorithm 1) is set to 10.0. We use 5 pyramid levels in all our experiments with a downsampling factor of 2.

3.1 Tests on Synthetic Data

Synthetic test data is created from an artificial vascular model, which is deformed in a length-preserving manner. Moreover, the deformation is chosen such that its major part occurs orthogonal to the image plane, see Fig. 3.

From this deformed model we compute a 2D projection using projection parameters from a calibrated C-arm device. The projected vascular model $\{(\mathbf{x}_i, r_i)\}$ is used to compute an artificial DSA image in the following way. We first use a background image, which contains noise and collimator masks similar to a real DSA. Then, we draw disks at each $\mathbf{x}_i$ with radius r_i. Intensities of disk pixels $\mathbf{x}_d$ are assigned proportional to the radius r_i:

$$\mathcal{I}(\mathbf{x}_d) = c - \frac{1}{2r_i}, \tag{14}$$

where c is an intensity constant, which represents the maximal value a contrasted vessel should have. This way we assure higher intensities at thin vessels and lower intensities at thicker vessels, which stems from the observation that X-rays get

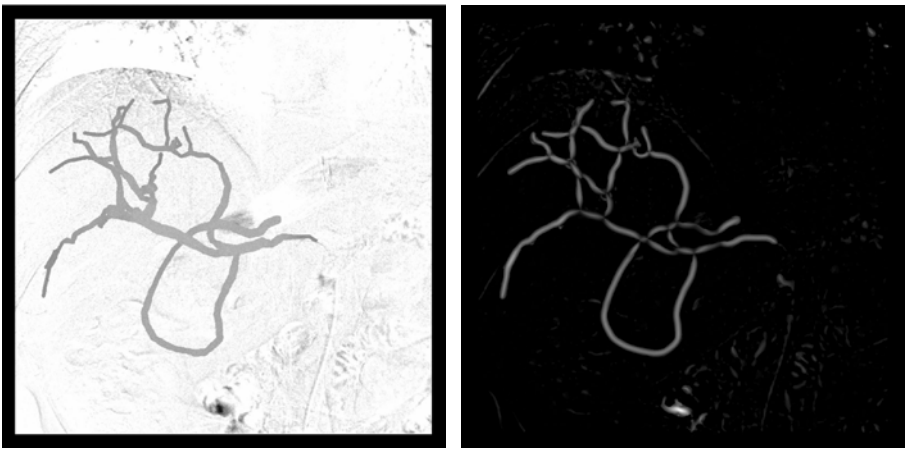

Fig. 4. A synthetic DSA created from the vasculature of an intraoperative CBR. The background image has been generated from two X-ray projections of the same patient. The right image shows the DSA after tubular structure enhancement. Note that, due to the background image, artifacts remain, which are similar to the ones in real DSA images.

more attenuated the more contrast agent they traverse, i.e. the thicker the vessel structure. Thereafter the intensities are smoothed using an averaging filter and Gaussian noise (with a standard deviation of 5% of the intensity range) is added.

We test three synthetic vascular models with increasing complexity and deformation, see Fig. 3. We compute Euclidean errors, angle errors, and runtime for our technique and for the feature-based approach. Input for the feature-based approach are the 2 vascular models $\{(\mathbf{X}_i, R_i)\}$, $\{(\mathbf{x}_i, r_i)\}$, and the projection function p. Table 1 illustrates errors with relative improvement compared to the initial situation as well as algorithm runtime in seconds.

3.2 Tests on Real Data

For the experiment similar to a clinical scenario we use two 3D data sets, a CTA, which has been acquired before an abdominal intervention, and a 3D CBR, which has been acquired with a C-arm during the intervention while a catheter was inserted. Both data sets visualize liver arteries of the same patient, which are extracted as described above to create two vascular models, $\{(\mathbf{X}_i^{CTA}, R_i^{CTA})\}$ and $\{(\mathbf{X}_i^{CBR}, R_i^{CBR})\}$. In a first step the two models are rigidly registered using a closed-form least-squares method [17] on manually assigned bifurcation correspondences. Then, more correspondences are manually assigned to compute a reference deformation via an interpolating TPS. The vascular model, which is extracted from the CBR, is projected using a calibrated projection matrix from the intraoperative C-arm. The projection matrix is chosen in anteroposterior position, which is a typical pose for the acquisition of DSA images during

Table 1. The first 6 rows show results on synthetic, the 2 lower rows on real data sets. Data with 'M2I' suffix show values for the proposed method, data with 'M2M' suffix show comparison values of the feature-based approach [1]. The second column shows the number of centerline points included in the 3D vascular model. The remaining rows show values for Euclidean and Angle error together with a relative improvement compared to the initial error as well as runtime (Intel Core2Duo 2.6GHz) results.

Data	$\lvert\{\mathbf{X_i}\}\rvert$	**Euclidean error** $[mm]$	**Angle error** $[rad]$	**Runtime** $[sec]$
S1-M2I	22	0.24 (77.7%)	0.04 (75.6%)	0.39
S1-M2M	22	0.31 (72.1%)	0.02 (85.5%)	2.67
S2-M2I	23	0.43 (68.0%)	0.07 (78.4%)	0.43
S2-M2M	23	0.40 (70.8%)	0.04 (88.7%)	3.27
S3-M2I	59	1.04 (26.7%)	0.34 (2.5%)	4.01
S3-M2M	59	0.86 (39.3%)	0.32 (6.7%)	17.90
R1-M2I	318	9.13 (16.3%)	0.22 (-0.2%)	184.1
R1-M2M	318	11.67 (-6.9%)	0.23 (-4.1%)	679.3

abdominal procedures. A synthetic DSA image is created from the projected vascular model as described above. Here, we obtain the background image by subtracting two high-dose X-ray images of the same patient, see Fig. 4. Again, tests were conducted using the proposed method and using the feature-based approach whose results are summarized in table 1.

Our experiments show that the new algorithm can cope with different deformations and has an accuracy similar to the feature-based approach. Moreover, when applied to the real data set, we improve the error by 16.3%, whereas the feature-based approach yields results worse than the initial situation. Please note that our algorithm decreases the runtime by a factor between 3 and 6 compared to the feature-based algorithm.

4 Conclusion

In this paper we propose a new method for deformable 2D-3D registration of vascular structures in a one-view scenario. Due to the combination of our novel image-based external energy term and a length preservation in 3D we create a well-posed problem, which can be solved via gradient descent optimization. Different to existing methods for 2D-3D non-rigid vascular registration, we define our energy on the image intensities, which both decreases runtime and increases ease of use. At the same time, we preserve accuracy as well as capture range due to a pyramidal implementation.

It should be noted that some approximative assumptions are made in our method. First, 3D centerlines are not projectively invariant, i.e. if registered, 3D

centerlines do not necessarily project onto centerlines extracted in 2D. Only if the center of the 3D vessel intersects with the principal ray[2], projected and 2D centerline would overlap. The same applies to the projection of radii as mentioned in Sec. 2.1: in general, the perspective projection of a ball is a conic, only in the aforementioned special case it becomes a disk. These two issues, however, are marginal since angiographic devices have a focal length, which is much larger than the extents of a volumetric data set. In such scenarios, the error which is introduced can be neglected. Finally, we leave the projected radius r_i constant throughout the optimization. When a centerline point is displaced the projection of its associated radius will also change, which consequently changes the size of the disks D_i, see Eq. (2). We also neglect this issue using the same argument as above.

Encouraged by the promising results we intend to run more extensive tests on real data, not only on abdominal but also on heart anatomy, where deformation is increased due to immanent heart beat.

References

1. Groher, M., Zikic, D., Navab, N.: Deformable 2d-3d registration of vascular structures in a one view scenario. IEEE Trans. Med. Imag. 28(6), 847–860 (2009)
2. Gorges, S., Kerrien, E., Berger, M.O., Trousset, Y., Pescatore, J., Anxionnat, R., Picard, L.: Model of a vascular C-Arm for 3D augmented fluoroscopy in interventional radiology. In: Duncan, J.S., Gerig, G. (eds.) MICCAI 2005. LNCS, vol. 3750, pp. 214–222. Springer, Heidelberg (2005)
3. Bender, F., Groher, M., Khamene, A., Wein, W., Heibel, T., Navab, N.: 3D dynamic roadmapping for abdominal catheterizations. In: Metaxas, D., Axel, L., Fichtinger, G., Székely, G. (eds.) MICCAI 2008, Part II. LNCS, vol. 5242, pp. 668–675. Springer, Heidelberg (2008)
4. Hipwell, J., Penney, G., McLaughlin, R., Rhode, K., Summers, P., Cox, T., Byrne, J., Noble, J., Hawkes, D.: Intensity based 2D-3D registration of cerebral angiograms. IEEE Trans. Med. Imag. 22, 1417–1426 (2003)
5. Turgeon, G.A., Lehmann, G., Guiraudon, G., Drangova, M., Holdsworth, D., Peters, T.: 2D-3D registration of coronary angiograms for cardiac procedure planning and guidance. Medical Physics 32, 3737–3749 (2005)
6. Jomier, J., Bullitt, E., van Horn, M., Pathak, C., Aylward, S.: 3D/2D model-to-image registration applied to TIPS surgery. In: Larsen, R., Nielsen, M., Sporring, J. (eds.) MICCAI 2006. LNCS, vol. 4191, pp. 662–669. Springer, Heidelberg (2006)
7. Metz, C.T., Schaap, M., Klein, S., Neefjes, L.A., Capuano, E., Schultz, C., van Geuns, R.J., Serruys, P.W., van Walsum, T., Niessen, W.J.: Patient specific 4D coronary models from ECG-gated CTA data for intra-operative dynamic alignment of CTA with X-ray images. In: Yang, G.-Z., Hawkes, D., Rueckert, D., Noble, A., Taylor, C. (eds.) MICCAI 2009. LNCS, vol. 5761, pp. 369–376. Springer, Heidelberg (2009)
8. Benameur, S., Mignotte, M., Parent, S., Labelle, H., Skalli, W., de Guise, J.: 3D/2D registration and segmentation of scoliotic vertebra using statistical models. Computerized Medical Imaging and Graphics 27, 321–337 (2003)

[2] The principal ray is the line, which connects the center of projection with the center of the image.

9. Tang, T.S.Y., Ellis, R.E.: 2D/3D deformable registration using a hybrid atlas. In: Duncan, J.S., Gerig, G. (eds.) MICCAI 2005. LNCS, vol. 3750, pp. 223–230. Springer, Heidelberg (2005)
10. Yao, J., Taylor, R.: Assessing accuracy factors in deformable 2D/3D medical image registration using a statistical pelvis model. In: International Conference on Computer Vision (ICCV), Washington, DC, USA, p. 1329. IEEE Computer Society, Los Alamitos (2003)
11. Rohr, K., Stiehl, H.S., Sprengel, R., Buzug, T.M., Weese, J., Kuhn, M.H.: Landmark-based elastic registration using approximating thin-plate splines. IEEE Trans. Med. Imag. 20(6), 526–534 (2001)
12. Chefd'hotel, C., Hermosillo, G., Faugeras, O.: Flows of diffeomorphisms for multimodal image registration. In: Proceedings of IEEE International Symposium on Biomedical Imaging, pp. 753–756 (2002)
13. Koller, T.M., Gerig, G., Szekely, G., Dettwiler, D.: Multiscale detection of curvilinear structures in 2-D and 3-D image data. In: International Conference on Computer Vision, ICCV (1995)
14. Rohr, K.: Landmark-based image analysis: using geometric and intensity models. Springer, Heidelberg (2001)
15. Nocedal, J., Wright, S.J.: Numerical Optimization. Springer, Heidelberg (2006)
16. Osher, S., Fedkiw, R.: Level Set Methods and Dynamic Implicit Surfaces. Springer, Heidelberg (2003)
17. Umeyama, S.: Least-squares estimation of transformation parameters between two point patterns. IEEE Trans. Pattern Anal. Mach. Intell (PAMI) 13(4), 376–380 (1991)